Am J Nucl Med Mol Imaging 2026;16(4):186-195
www.ajnmmi.us /ISSN:2160-8407/ajnmmi0172827

Original Article

A functional view on the enhanced therapeutic effects of the control-released recombinant human endostatin

Xuyu Zhang[1], Kun Zhao[1], Kaining Yang[1], Xiao Li[2], Fengcai Li[1], Jiahua Zhou[3], Ni Wang[2], Yanli Wang[1]

[1]Baoding Second Central Hospital, Baoding 072750, Hebei, China; [2]Shanghai Institute of Applied Physics, Chinese Academy of Science, Shanghai 201800, China; [3]Department of Medical Oncology, Shanghai Jiangong Hospital, Shanghai 200083, China

Received March 23, 2026; Accepted August 16, 2026; Epub August 25, 2026; Published August 30, 2026

Abstract: Recombinant human endostatin (RHE) has been applied in treating non-small cell lung cancer via inhibiting tumor neovascularization. In this study, a controlled release of RHE was proposed and manifested in a fluorescent view. In a mice model with NSCLC xenografts, the prolonged pharmacokinetics curves and pharmaceutic concentrations in tumor contributed to the inhibition of neovascularization that was proved with ^{68}Ga-RGD PET, and finally reflected as the delayed tumor growth rate. Conclusively, the functional view on the basis of molecular imaging can exhibit the procedure and outcome of the controlled release of RHE, which can effectively enhance the therapeutic effects in treating NSCLC.

Keywords: Recombinant human endostatin, neovascularization, controlled release, non-small cell lung cancer, ^{68}Ga-RGD PET

Introduction

Recombinant human endostatin (RHE) is an anti-angiogenic biological product developed for tumor therapy [1]. Its primary mechanism involves inhibiting the migration of vascular endothelial cells [2], which suppresses tumor neovascularization, blocks the nutrient supply to tumor cells, and ultimately inhibits tumor proliferation and metastasis.

Controlled drug release is a critical strategy to optimize therapeutic efficacy. This can be achieved through various systems, broadly categorized by mechanism into diffusion-controlled, chemically controlled, and solvent-activated systems [3, 4]. Polymeric nanoparticles and nanoliposomes are examples of nanocarriers whose drug-release behavior is governed mainly by diffusion or solvent activation [5, 6]. Controlled-release formulations are convenient to administer and help maintain stable plasma drug concentrations. By limiting drug accumulation, these systems may reduce toxicity and adverse effects in normal tissues, thereby improving therapeutic efficacy [7-9].

The choice of drug-delivery route can affect both therapeutic efficacy and patient adherence. Intravenous infusion ports provide long-term venous access for drug administration, transfusion, and nutritional support. Compared with peripherally inserted central catheters, these devices may offer lower infection rates, improved safety, and greater patient acceptance [10]. Treatment efficacy also depends on the infusion regimen. Cell cycle-nonspecific drugs are commonly administered as bolus injections, whereas cell cycle-specific agents, such as endostatin, are generally delivered by slow intravenous infusion to maximize their therapeutic effects [11].

Advances in tumor biology have enabled more precise treatment strategies. Vascular endothelial growth factor (VEGF) regulates vasculogenesis and angiogenesis [12], and its expression increases substantially in stromal cells during tumor development [13]. Binding of VEGF to tyrosine kinase receptors, including VEGFR-1 and VEGFR-2, promotes endothelial-cell migration, proliferation, and tubule formation. It also increases vascular permeability [14]. These effects make VEGF a suitable target for therapeutic intervention [15]. For instance, a meta-analysis by Papathanassiou et al. showed that both topical instillation and subconjunctival injection of the anti-VEGF agent bevacizumab significantly reduced corneal neovascularization, with topical administration showing superior efficacy [16]. Beyond VEGF inhibition, other endogenous inhibitors are being explored. Canstatin, a recently identified angiogenesis inhibitor, has shown promise in preclinical models. In a rat model of alkali burn-induced neovascularization, daily intraperitoneal injections of recombinant canstatin (5 mg/kg or 10 mg/kg for 14 days) inhibited neovascularization and significantly decreased the expression of VEGF and tumor necrosis factor-alpha (TNF-α) [17].

Angiogenesis is fundamental to the growth, metastasis, and prognosis of malignant solid tumors [18, 19]. Therefore, strategies like controlled-release formulations of endostatin and targeted inhibition of pathways like VEGF represent a rational and effective approach to cancer therapy.

https://doi.org/10.62347/DJEZ7112

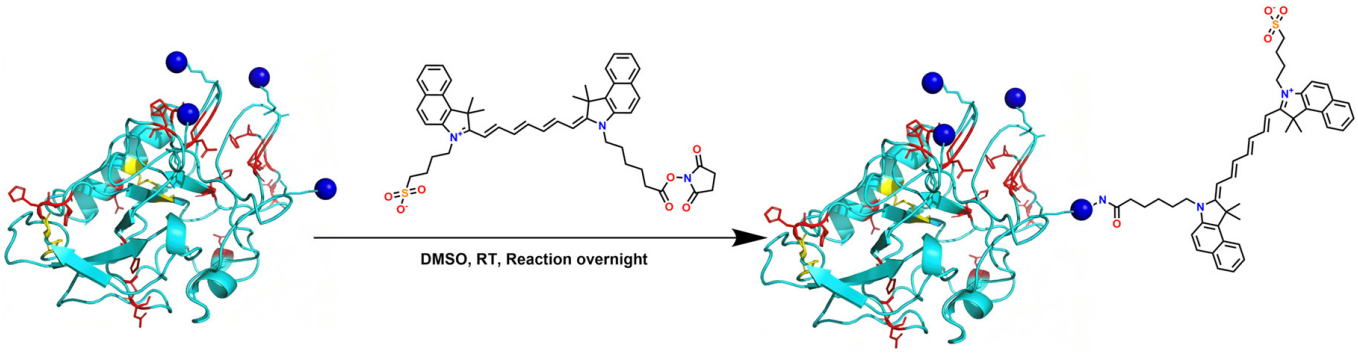

Scheme 1. Schematic procedure of the synthesis of RHE.

In the present study, we hypothesized that a Matrigel-based sustained-release formulation of RHE would achieve prolonged local retention and enhanced anti-angiogenic efficacy compared with conventional daily administration. To test this hypothesis, we employed multimodal molecular imaging - including fluorescence imaging for pharmacokinetic assessment and ^{68}Ga-RGD/^{18}F-FDG PET for functional evaluation of angiogenesis and glucose metabolism - in an A549 NSCLC xenograft mouse model. Our findings demonstrate that sustained RHE release significantly inhibits tumor neovascularization, reduces tumor glucose metabolism, and delays tumor growth, providing functional evidence for the therapeutic advantage of controlled-release anti-angiogenic therapy.

Materials and methods

Materials and reagents

RHE injection (Shandong Xiansheng Biopharmaceutical Co., Ltd., Lot No. 202208040), NHS-ICG (Meiluo Technology Co., Ltd. Lot No. 380201), Matrix gel (Corning Incorporated, Cat# 354234).

Preparation of animal models

Human non-small cell lung cancer A549 cell line was purchased from Shanghai Chuanqiu Biotechnology Co., Ltd. (Shanghai, China). The cells were seeded in T25 cell culture flasks containing 5 mL of F12K medium supplemented with 10% fetal bovine serum (FBS). The flasks were maintained in a humidified incubator at 37°C with 5% CO_2. Cell growth was monitored daily. Upon reaching the exponential growth phase, the cells were harvested. The cell suspension was then diluted with PBS to adjust the final concentration to 1 × 10^8 cells/mL for subsequent experiments.

All animal procedures were approved by the Animal Ethics Committee of Baoding Second Central Hospital (approval no. 2022-66) and were performed in accordance with applicable guidelines and regulations. This study was reported in accordance with the ARRIVE guidelines.

Female athymic nude mice (aged 6-8 weeks) were obtained from SPF (Beijing) Biotechnology Co., Ltd. Animals were housed under specific pathogen-free conditions at 20-24°C with a 12-hour light/dark cycle and given at least 7 days for acclimatization before the experiment. Exponentially growing A549 cells were harvested, resuspended in PBS, and mixed 1:1 (v/v) with Matrigel on ice. Each mouse received a 100 μL subcutaneous injection of the cell-Matrigel suspension into the right flank, corresponding to 5 × 10^6 cells. Tumor growth was monitored daily, and tumor volume (TV) was measured every two to three days using a caliper. Tumor TV was estimated as $V = 0.5 \times L \times W^2$, where L is the longest tumor diameter and W is the perpendicular shorter diameter. When the mean TV reached approximately 60 mm^3 (typically 10-14 days post-inoculation), mice with uniform tumor size and shape were selected for subsequent treatment experiments. At this point, mice were randomly assigned to different treatment groups based on TV to ensure comparable baseline tumor sizes across groups.

Fluorescence characterizes metabolism in vivo with different modes of administration

Conjugation of RHE with NHS-ICG (**Scheme 1**): RHE (200 μL, 5 mg/mL) was transferred to a 2 mL microcentrifuge tube. Subsequently, 0.9 mg of NHS-ICG (dissolved in 50 μL of DMSO) was added to the tube. The conjugation reaction was allowed to proceed overnight at room temperature with continuous stirring, protected from light. The resulting NHS-ICG-labeled RHE was purified by ultrafiltration using a 10 kDa molecular weight cut-off (MWCO) centrifugal filter unit to remove unbound dye. The purified ICG-RHE conjugate was then collected for subsequent experiments. The protein model prediction for RHE was generated by SWISS-MODEL (https://www.expasy.org/resources/swiss-model).

RHE integrity was assessed using a SRT-C SEC 300A chromatography column (4.6 × 300 mm, Sepax Technologies Co., Ltd., USA). RHE was detected separately via HPLC with test conditions as below: mobile phase, 150 mM PBS (pH = 7.0); flow rate, 0.35 mL/min; detection wavelength, 214 nm; injection volume, 20 μL.

Fluorescence verification of administration mode

Male athymic nude mice (5-week-old) were randomly divided into three groups (n = 3 per group). Mice in Group 1 (SC-Matrigel) received a subcutaneous injection of 100 μL Matrigel containing RHE-ICG. Group 2 (SC-Saline) received a subcutaneous injection of 100 μL normal saline containing RHE-ICG. Group 3 (IV-Saline) received an intravenous injection (via tail vein) of 100 μL normal saline containing RHE-ICG. At predetermined time points post-injection (0.5, 1, 2, 4, 6, 24, 32, 48, 72, and 120 h), mice were anesthetized and imaged using the VISQUE® Invivo Smart-LF small animal imaging system (Vieworks Co., Ltd., Korea). The total fluorescence intensity in the muscle region of interest (ROI) at each time point was quantitatively analyzed using the VISQUE Invivo Smart LF software.

Radiolabeling of RHE with ^{125}I for pharmacokinetic evaluation

RHE was radiolabeled with $Na^{125}I$ using the chloramine-T method. For radiolabeling, Iodogen® solution (200 μL, 2 mg/mL in chloroform) was added to a glass tube and evaporated under nitrogen to generate an Iodogencoated surface. RHE (100 μg) and $Na^{125}I$ were added and incubated at 37°C for 30 min.

Radiochemical purity (RCP) was evaluated by radio-thin-layer chromatography (Radio-TLC) using instant TLC-SG glass microfiber chromatography paper (Agilent Technologies, Santa Clara, CA, USA) with dichloromethane/methanol (10:1, v/v) as the mobile phase. The R_f value of ^{125}I-RHE was approximately 0.8-1.0.

Pharmacokinetic study of ^{125}I-RHE

For the pharmacokinetic study, tumor-bearing mice received subcutaneous injections of ^{125}I-RHE either in Matrigel (sustained-release group, n = 3) or in normal saline (conventional group, n = 3). Blood samples were collected from the tail vein at 0.25, 0.5, 1, 2, 4, 12 and 24 h post-injection. Radioactivity in each blood sample was measured using a γ-counter (JC-2101, Beijing PET Technology Co., Ltd.). The measured counts were decay-corrected to the injection time and converted to percentage of injected dose per gram of blood (%ID/g) to construct the blood clearance curves.

Growth inhibition of NSCLC with sustained RHE-release

Athymic nude mice bearing A549 tumors (approximately 60 mm^3) were randomly assigned to three groups: control group (n = 4), SC-Matrigel group (n = 3), and SC-Saline group (n = 3). The day of treatment initiation was designated as day 0. Group A received a subcutaneous injection of a mixture containing 24 μL of RHE stock solution and 76 μL of Matrigel every 4 days. SC-Saline received a daily subcutaneous injection of a mixture containing 6 μL of RHE stock solution and 94 μL of normal saline. The control group received an equal volume of normal saline via the same subcutaneous route.

General health status of the mice, including mental state, activity level, body weight, and food/water intake, was monitored daily throughout the study. Tumor growth was monitored every three days starting from day 1 post-treatment. TV was measured using a caliper. On day 25, the TV inhibition rate (TIR) was calculated using the following formula: TIR (%) = [(mean $TV_{control}$ - mean $TV_{treatment}$)/mean $TV_{control}$] × 100%.

Molecular imaging recording of sustained RHE-release

PET imaging tests were performed 15 days after administration of RHE. ^{18}F-FDG was obtained from Shanghai Atom Kexing Pharmaceuticals Co., Ltd. ^{68}Ga-RGD was prepared in-house using a commercial labelling kit (Shanghai Nice-Labeling Biotechnology Co., Ltd.).

For ^{68}Ga-RGD PET/CT, tumor-bearing mice were anaesthetized with isoflurane and intravenously injected with 3.7 MBq of tracer per mouse. Body weight was recorded immediately before each PET scan for SUV calculation. Scans were acquired 45 min after injection using a clinical PET/CT scanner (Biograph 64, Siemens, Germany). Each PET acquisition was followed by low-dose CT imaging. CT parameters were as follows: tube voltage: 120 kV; tube current: 35 mA; pitch: 1.0; and reconstructed slice thickness, 2 mm. Whole-body PET images were obtained over two bed positions, with an acquisition time of 3 min per bed. Images were reconstructed using the TrueD system to generate axial, coronal, sagittal, and three-dimensional projection images. Tumor regions of interest (ROI) were manually delineated by a nuclear medicine physician. Provided maximum standardized uptake value (SUV_{max}) as the quantitative results. SUV_{mean} was also calculated as an additional quantitative metric alongside SUV_{max}, as SUV_{mean} is less susceptible to partial volume effects and noise compared with SUV_{max}, particularly in small-volume tumors. The standardized uptake value (SUV) was calculated as the ratio of tissue radioactivity concentration (kBq/mL) to the injected dose per body weight (MBq/kg). Body weight was measured immediately before each PET scan. A nuclear medicine physician was responsible for identifying ROIs and measuring tumor SUV_{max} and SUV_{mean}.

^{18}F-FDG PET/CT was performed with an interval of 8 h during that the mice were kept fasting. The same acquisition and reconstruction procedures used for ^{68}Ga-RGD PET/CT were applied, with the scanner configured for ^{18}F acquisition.

Histopathological analysis

On day 25, mice were anaesthetized with 3% pentobarbital sodium (70 mg/kg, intraperitoneal injection) and then euthanized by cervical dislocation. Samples for histological analysis were fixed in 4% paraformaldehyde, paraffin embedded, and sectioned at 4 μm. Haematoxylin and eosin (H&E) staining was performed to evaluate tumor morphology.

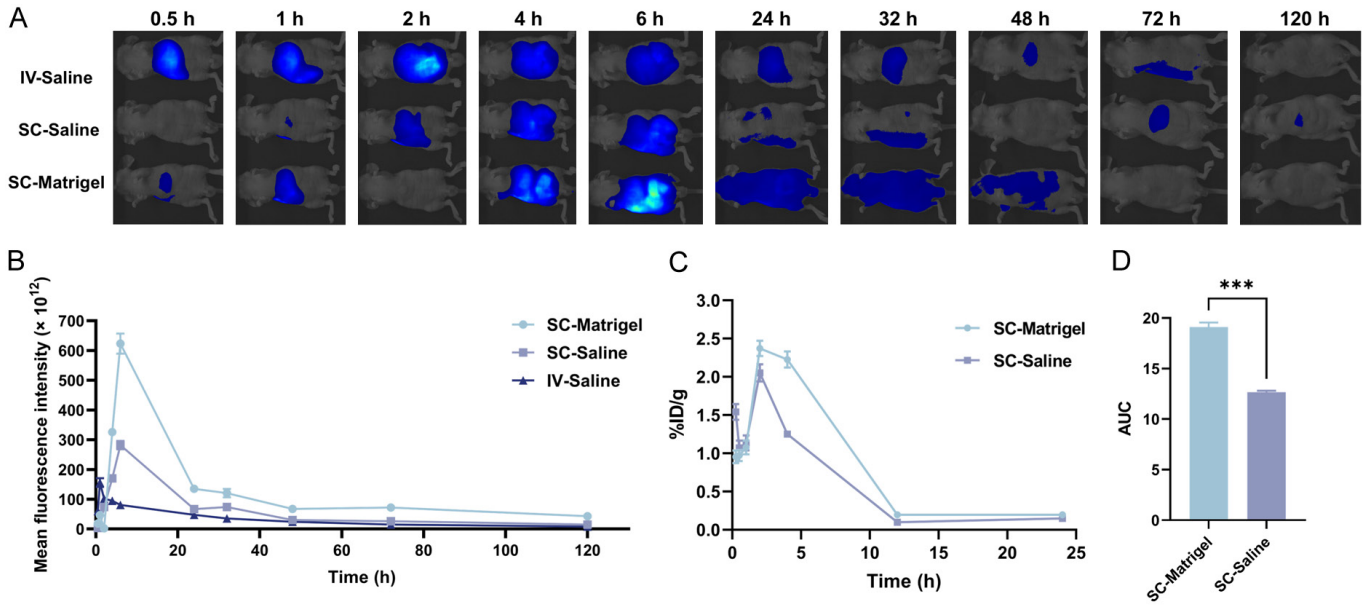

Figure 1. In vivo fluorescence imaging of RHE-ICG distribution following different administration routes. A. Representative fluorescence images of NTG mice at indicated time points (0.5, 1, 2, 4, 6, 24, 32, 48, 72, and 120 h) post-injection. Group 1: subcutaneous injection with matrigel (SC-Matrigel); Group 2: subcutaneous injection with normal saline (SC-Saline); Group 3: intravenous injection with normal saline (IV-Saline). B. Quantitative analysis of mean fluorescence intensity in the muscle region of interest over time. Data are presented as mean ± SD (n = 3 per group). C. Pharmacokinetic profiles of ^{125}I-labeled RHE following SC-Matrigel or SC-Saline. D. AUC of ^{125}I-labeled RHE following SC-Matrigel or SC-Saline.

Immunohistochemical (IHC) staining was used to determine the expression of VEGF, TNF-α, Ki67, and BAX in tumor tissues. Stained sections were examined using an inverted fluorescence microscope. Images were analyzed with Image-Pro Plus software, version 6.0.0.260 (Media Cybernetics Corporation, USA). Relative protein expression was quantified as average optical density (AOD), calculated by dividing the integrated optical density by the total area of the ROI.

Statistical analysis

Statistical calculations and data analysis were performed using GraphPad Prism (version 9.5.1; Graphpad Software, USA). The data are presented as means ± standard deviations (SDs). Differences between two groups were analysed using Student's t test, whereas one-way analysis of variance was applied to comparisons involving multiple groups. A two-sided *P* value of < 0.05 was considered statistically significant. All experiments were conducted in triplicate.

Results

Evaluation of sustained-release effect based on fluorescence imaging

The successful conjugation of RHE with NHS-ICG was confirmed by HPLC (Figure S1). To investigate the release kinetics of RHE-ICG following different administration routes, we monitored the fluorescence signal in the muscle region over 120 h post-injection.

As shown in **Figure 1A**, the three groups displayed different fluorescence-retention patterns. The SC-Matrigel formulation maintained detectable fluorescence for up to 120 h, with signal intensity reaching a maximum at approximately 6 h before gradually declining, consistent with sustained release from the Matrigel depot. In comparison, fluorescence following subcutaneous saline injection decreased rapidly and was nearly undetectable by 48 h, whereas intravenous administration produced an earlier peak (1 h) followed by almost complete clearance within 24 h. Modest inter-animal variability in fluorescence distribution was observed at 2 h, likely reflecting differences in injection placement or local absorption (**Figure 1A**).

Quantitative ROI analysis further showed prolonged local retention of RHE-ICG in the SC-Matrigel group relative to both saline-treated groups throughout the 4-120 h observation period ($P < 0.01$; **Figure 1B**), supporting the role of Matrigel as an effective sustained-release depot for local RHE delivery.

To further validate the sustained-release profile, pharmacokinetic analysis was performed using ^{125}I-labeled RHE. As shown in **Figure 1C**, the Matrigel-based sustained-release formulation significantly prolonged the blood circulation time of ^{125}I-RHE compared with the conventional subcutaneous injection. The area under the curve (AUC) was significantly greater in the sustained-release group, indicating enhanced systemic exposure and prolonged drug availability (**Figure 1D**). These findings provide direct pharmacokinetic evidence that Matrigel encapsulation effectively sustains the release of RHE, consistent with the fluorescence imaging results.

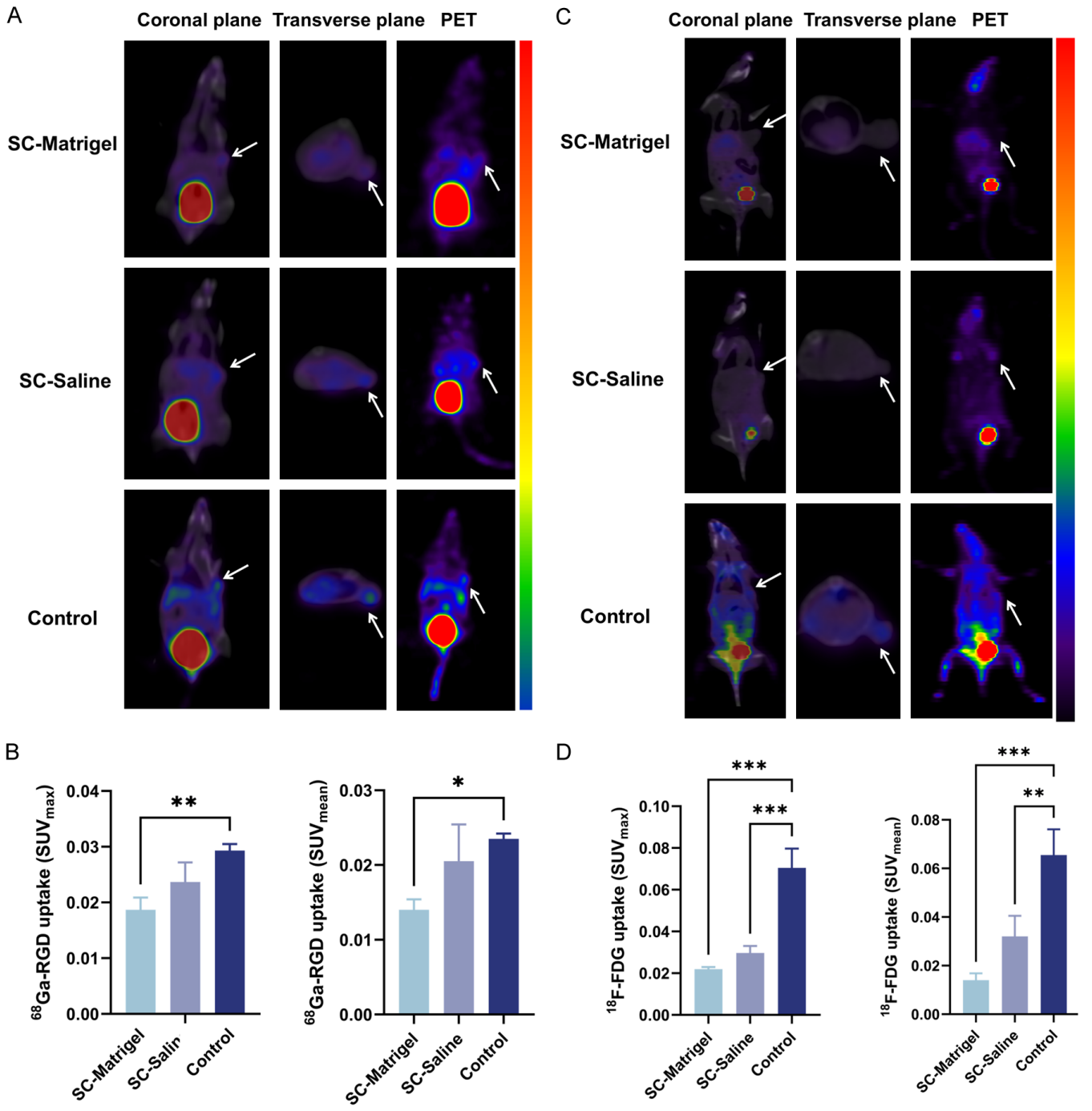

Figure 2. Molecular imaging assessment of angiogenesis and glucose metabolism on day 15 post-treatment. A. Representative ^{68}Ga-RGD PET/CT images of tumors from each group. B. Quantitative analysis of ^{68}Ga-RGD uptake expressed as maximum standardized uptake value (SUV_{max}) and mean standardized uptake value (SUV_{mean}). C. Representative ^{18}F-FDG PET/CT images of tumors from each group. D. Quantitative analysis of ^{18}F-FDG uptake expressed as SUV_{max} and SUV_{mean}. Data are presented as mean ± SD (n = 3 per group). *P < 0.05, **P < 0.01, and ***P < 0.001: differences between control and other groups.

Molecular imaging assessment of angiogenesis and glucose metabolism

To investigate the functional basis of enhanced antitumor efficacy, we performed PET imaging using ^{68}Ga-RGD (targeting integrin αvβ3 as a marker of angiogenesis) and ^{18}F-FDG (assessing glucose metabolism) on day 15 post-treatment initiation.

Representative PET images and quantitative SUV_{max} analysis are presented in **Figure 2**. SC-Matrigel demonstrated the lowest ^{68}Ga-RGD uptake in tumors (SUV_{max}: 0.019 ± 0.003; SUV_{mean}: 0.014 ± 0.002), which was significantly lower than that of the control group (SUV_{max}: 0.029 ± 0.001; SUV_{mean}: 0.024 ± 0.001) (P < 0.05). Although SC-Saline also showed reduced uptake compared to the control group (SUV_{max}: 0.024 ± 0.005; SUV_{mean}: 0.021 ±

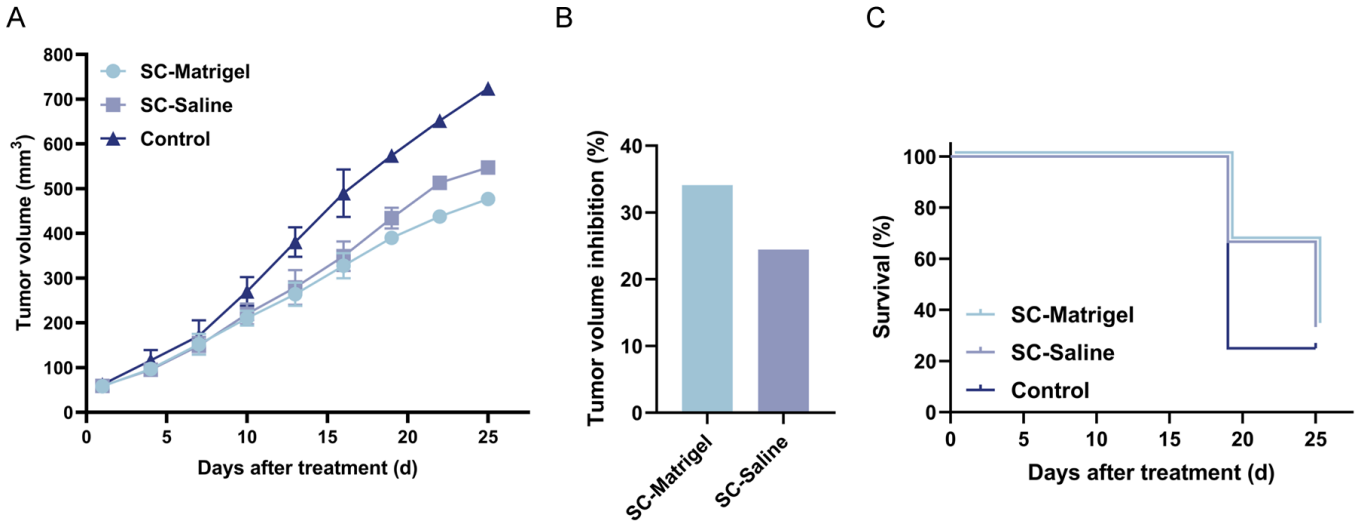

Figure 3. Antitumor efficacy of different RHE administration regimens in A549 tumor-bearing NTG mice. A. Tumor growth curves over 25 days post-treatment initiation. B. Tumor volume inhibition rate on day 25. C. Kaplan-Meier survival of different RHE administration. Data are presented as mean ± SD (control, n = 4; SC-Matrigel, n = 3; SC-Saline, n = 3).

0.005), no statistically significant difference was observed between SC-Matrigel and SC-Saline (**Figure 2A**, **2B**). This indicates that sustained-release RHE formulation more effectively inhibited tumor neovascularization. The reduced ^{68}Ga-RGD signal correlates with the observed tumor growth inhibition, consistent with the anti-angiogenic mechanism of endostatin.

^{18}F-FDG PET imaging revealed a similar pattern, with SC-Matrigel showing the lowest tumor glucose metabolism (SUV_{max}: 0.022 ± 0.001; SUV_{mean}: 0.014 ± 0.003), followed by SC-Saline (SUV_{max}: 0.030 ± 0.003; SUV_{mean}: 0.032 ± 0.008) and control group (SUV_{max}: 0.071 ± 0.009; SUV_{mean}: 0.066 ± 0.010) ($P < 0.01$, **Figure 2C**, **2D**). The reduced metabolic activity in SC-Matrigel likely reflects the consequences of impaired vascular supply and subsequent tumor cell starvation.

Enhanced antitumor efficacy of sustained-release RHE formulation

To evaluate whether the sustained-release profile translates into improved therapeutic outcomes, we compared the antitumor efficacy of RHE administered via different regimens in A549 tumor-bearing NTG mice.

As shown in **Figure 3**, tumor growth curves revealed significant differences among the treatment groups. SC-Matrigel (n = 3) exhibited the most pronounced tumor growth inhibition, with mean tumor volume reaching 477.00 ± 5.67 mm^3 on day 25, compared to 547.00 ± 8.21 mm^3 in SC-Saline (n = 3) and 724.00 ± 8.55 mm^3 in the control group (n = 4) ($P < 0.01$, **Figure 3A**). The TIR on day 25 was 34.12% for SC-Matrigel and 24.45% for SC-Saline (**Figure 3B**). Kaplan-Meier survival analysis was performed over the 25-day treatment period. All animals (control, n = 4; SC-Matrigel, n = 3; SC-Saline, n = 3) survived until day 16 regardless of treatment. On day 19, the survival rate dropped to 25% (1/4) in the control group, whereas both the SC-Matrigel and SC-Saline groups maintained 67% (2/3) survival. At the study endpoint (day 25), the survival rates were 33% (1/3) for both treatment groups, compared to 25% (1/4) for the control group, suggesting a potential survival benefit associated with RHE treatment (**Figure 3C**).

Longitudinal monitoring of general health status showed no significant differences in body weight, food intake, or activity levels among the three groups throughout the study period, suggesting that both treatment regimens were well-tolerated.

Histopathological and IHC analysis

Histopathological examination on day 25 revealed distinct morphological differences among the groups (**Figure 4A**). H&E staining showed extensive areas of cellular necrosis and cavity formation in tumor tissues from SC-Matrigel and, to a lesser extent, SC-Saline. In contrast, tumors from the control group exhibited relatively intact cellular architecture with minimal necrosis.

VEGF staining was more intense in both treatment groups than in the control group, with the strongest signal observed in SC-Matrigel tumors (**Figure 4A**). Consistent with this result, VEGF AOD was significantly higher in both treatment groups than in controls ($P < 0.001$), and was greatest in the SC-Matrigel group (**Figure 4B**). Increased VEGF expression after antiangiogenic treatment may reflect a compensatory response to hypoxia within the tumor microenvironment. Reduced vascular supply can restrict nutrient availability and may induce tumor cells to increase angiogenic-factor expression.

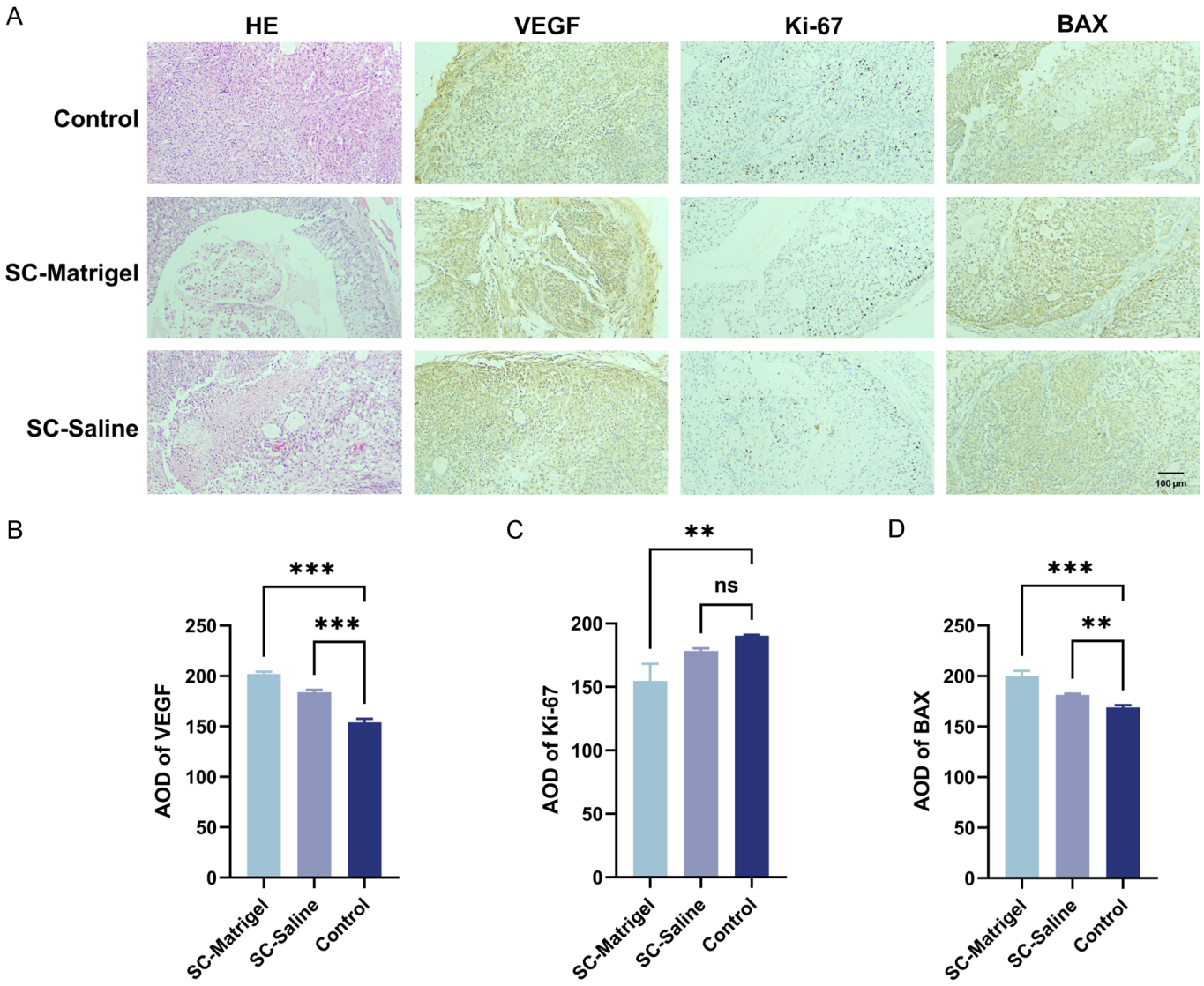

Figure 4. Histopathological and IHC analysis of tumor tissues on day 25. A. Representative images of H&E staining, and IHC staining for VEGF, Ki67, and BAX in tumor sections from each group. Scale bar = 100 μm. B. Quantitative analysis of VEGF expression expressed as AOD. C. Quantitative analysis of Ki67 proliferation index expressed as AOD. D. Quantitative analysis of BAX expression expressed as AOD. Data are presented as mean ± SD. Statistical comparisons were performed using one-way ANOVA. $*P < 0.05$, $**P < 0.01$, and $***P < 0.001$ indicate significant differences between control and other groups. AOD was calculated by dividing the integrated optical density by the total area of the region of interest, reflecting the relative expression level of each target protein.

Ki67 staining differed across the three groups. In SC-Matrigel tumors, proliferative activity was concentrated at the tumor periphery. In the SC-Saline group, Ki67-positive foci appeared at both the margins and central regions. Control tumors showed diffuse, high Ki67 expression throughout the tissue (**Figure 4A**). This heterogeneous distribution may be related to differences in drug penetration and regional treatment response. Ki67 AOD was significantly lower in the SC-Matrigel group than in controls ($P < 0.01$), whereas the SC-Saline group showed an intermediate level (**Figure 4C**).

BAX staining was most prominent in SC-Matrigel tumors, particularly near necrotic regions. SC-Saline tumors showed moderate BAX expression, while control tumors showed little apoptotic signal (**Figure 4A**). Quantitative analysis confirmed that BAX AOD was significantly higher in SC-Matrigel tumors than in control tumors ($P < 0.001$; **Figure 4D**). Together, these findings suggest that the sustained-release RHE formulation inhibits angiogenesis and promotes tumor-cell apoptosis.

Discussion

Recombinant human endostatin has been clinically applied for non-small cell lung cancer treatment through its anti-angiogenic mechanism [1, 20-22]. However, the short half-life of RHE necessitates frequent administration, which may impact patient compliance and therapeutic consistency. In the present study, we developed

a Matrigel-based sustained-release formulation of RHE and evaluated its pharmacokinetic profile and therapeutic efficacy using multimodal molecular imaging approaches.

Our fluorescence imaging results show that Matrigel-encapsulated RHE-ICG exhibits significantly prolonged local retention compared to conventional subcutaneous or intravenous administration. The sustained release profile, with detectable signals persisting up to 120 h, matches the design principles of long-acting drug delivery systems that maintain therapeutic drug levels within the optimal concentration window [23-25]. Matrigel, as a basement membrane matrix, provides a biodegradable depot that gradually releases encapsulated proteins through diffusion and matrix degradation [12]. This was further confirmed by our ^{125}I-RHE pharmacokinetic study, which demonstrated significantly increased AUC in the sustained-release group, providing direct evidence that Matrigel encapsulation effectively prolongs RHE circulation. This approach addresses a major limitation of anti-angiogenic proteins, their short biological half-life and the need for frequent administration [13].

The improved antitumor efficacy observed in SC-Matrigel (Matrigel formulation administered every 4 days) compared to SC-Saline (daily conventional injections) shows that sustained release, rather than cumulative dose alone, determines therapeutic outcome. Although the total RHE dose over 25 days was comparable between groups (150 μL in SC-Matrigel vs. 150 μL in SC-Saline), the sustained-release formulation achieved superior tumor growth inhibition. This finding supports the concept that maintaining continuous angiogenic suppression is more effective than intermittent high-concentration exposure [26, 27]. Previous studies have similarly shown that prolonged endostatin therapy can maintain tumors in a state of dormancy [22].

The molecular imaging results provide functional insights into the mechanisms underlying improved efficacy. ^{68}Ga-RGD PET, targeting integrin αvβ3 expressed on activated endothelial cells, acts as a non-invasive biomarker of angiogenesis [28-30]. The significantly reduced ^{68}Ga-RGD uptake in SC-Matrigel tumors shows more effective suppression of neovascularization by the sustained-release formulation. The inclusion of SUV_{mean} as an additional quantitative metric, which is less susceptible to partial volume effects, further supports the robustness of this finding. This finding corroborates previous reports that continuous endostatin exposure achieves greater anti-angiogenic effect than intermittent administration. The concomitant reduction in ^{18}F-FDG uptake reflects the metabolic consequences of vascular inhibition, as tumor cells deprived of adequate blood supply exhibit decreased glucose utilization [31]. The combination of both tracers allows us to establish a mechanistic link between angiogenic inhibition and tumor metabolic response, strengthening the evidence that sustained RHE release exerts its antitumor effect through vascular disruption rather than direct cytotoxicity.

The IHC findings reveal complex adaptive responses within the tumor microenvironment. Increased VEGF expression in treatment groups, despite effective angiogenesis inhibition, likely represents a hypoxia-driven compensatory mechanism. Tumor cells responding to vascular suppression upregulate pro-angiogenic factors in an attempt to restore perfusion, a phenomenon previously described in anti-angiogenic therapy. In SC-Matrigel tumors, Ki67-positive cells were mainly confined to the tumor margins. This distribution may be consistent with improved drug penetration and more uniform suppression of proliferation in central tumor regions following sustained RHE release, compared with conventional administration.

The higher number of BAX-positive cells in SC-Matrigel tumors suggests that sustained RHE release may promote apoptosis in addition to its antiangiogenic activity. Endostatin can induce apoptosis directly in endothelial cells and indirectly in tumor cells through vascular disruption [32], which may contribute to the improved antitumor efficacy of the sustained-release formulation.

Although this study provides proof-of-concept evidence for this sustained delivery strategy, several limitations should be noted. A Matrigel-only control group was not included, so carrier-related effects could not be assessed directly. However, the antitumor effects observed in this study are unlikely to be explained by the carrier alone, as consistent treatment responses were observed across tumor growth, PET imaging, and histological analyses. The survival analysis involved few animals and a short follow-up period; therefore, the findings should be interpreted cautiously. Nevertheless, the survival trend was consistent with the overall therapeutic responses observed in tumor growth, PET imaging, and histological analyses. Use of a clinical PET scanner for small-animal imaging may have affected absolute SUV quantification through partial-volume effects. Because identical imaging and reconstruction protocols were applied across groups, relative comparisons between treatments remain informative. Finally, although Matrigel was an effective proof-of-concept depot, its biological origin limits clinical translation. Future studies should focus on clinically translatable sustained-release biomaterials.

Notwithstanding these limitations, our study shows that molecular imaging provides a powerful tool for visualizing and quantifying the functional consequences of controlled-release drug delivery. The integration of fluorescence imaging for pharmacokinetic assessment and PET imaging for pharmacodynamic evaluation offers a comprehensive platform for optimizing drug formulation strategies.

Conclusion

In conclusion, sustained local delivery of recombinant human endostatin through a Matrigel-based depot significantly enhanced antitumor efficacy compared with conventional daily administration without increasing the total drug dose. Prolonged local retention resulted in sustained suppression of tumor angiogenesis, suggesting that treatment efficacy depends more on continuous anti-angiogenic pressure than on cumulative drug exposure. Furthermore, multimodal molecular imaging enabled dynamic, noninvasive evaluation of both drug retention and therapeutic response, providing complementary information that cannot be obtained from tumor volume measurements alone. These findings not only support sustained-release strategies for anti-angiogenic therapy but also highlight molecular imaging as a valuable tool for the development and optimization of controlled-release drug delivery systems.

Acknowledgements

This work was supported by the science and technology project of Baoding (No. 2241ZF203) and the Key Project of Frontier Technology, Shanghai Institute of Applied Physics, Chinese Academy of Sciences (SINAP-QYJS-202401).

Disclosure of conflict of interest

None.

Address correspondence to: Jiahua Zhou, Department of Medical Oncology, Shanghai Jiangong Hospital, No. 666 Zhongshan North 1st Road, Shanghai 200083, China. Tel: +86-021-65313760; E-mail: xindianwukuang@hotmail.com; Ni Wang, Shanghai Institute of Applied Physics, Chinese Academy of Science, 2019 Jialuo Highway, Shanghai 201800, China. Tel: +86-021-59553998; E-mail: wangni@sinap.ac.cn; Yanli Wang, Baoding Second Central Hospital, No. 57 Fanyang Middle Road, Baoding 072750, Hebei, China. Tel: +86-0312-3966001; E-mail: msg_wang@sina.com

References

[1] Zhong Q, Tao Y, Chen H, Zhou Y, Huang L, Han X and Shi Y. The changing landscape of anti-lung cancer drug clinical trials in mainland China from 2005 to 2020. Lancet Reg Health West Pac 2021; 11: 100151.

[2] Liu Y, Liu HG and Zhao C. Intraperitoneal perfusion of endostatin improves the effectiveness and prolongs the prognosis of patients with gastric cancer. World J Gastrointest Oncol 2025; 17: 103131.

[3] Ayaz H, Khan A, Khan N, Hasnain M, Mesbah S, Ahmad A, Ahmed M, Ayaz H, Ahmed R and Sana A. Smart drug delivery systems: current technologies, clinical applications, and future perspectives in precision therapeutics. International Journal of Scientific Research and Modern Technology 2025; 4: 18-38.

[4] Adepu S and Ramakrishna S. Controlled drug delivery systems: current status and future directions. Molecules 2021; 26: 5905.

[5] El-Khawaga AM, Youssef OI, El-Dydamoni OA, Ragab WM and Mohammed RAE. Advances in green-synthesized magnetic nanoparticles for targeted cancer therapy: mechanisms, applications, and future perspectives. Eur J Med Res 2026; 31: 347.

[6] Hasan N, Aftab M, Ikram S, Mustofa AZ, Sriwidodo S, Darusman HS, Amir MN, Tockary TA and Uchida S. Recent advances in lipid nanoparticles for cancer vaccine delivery: challenges and future perspectives. Int J Pharm X 2026; 11: 100484.

[7] Wu M, Xia T, Li Y, Wang T, Yang S, Yu J, Liang Q, Shen T, Yu M and Zhao B. Design and fabrication of r-hirudin loaded dissolving microneedle patch for minimally invasive and long-term treatment of thromboembolic disease. Asian J Pharm Sci 2022; 17: 284-297.

[8] Li W, Chen J, Zhao S, Huang T, Ying H, Trujillo C, Molinaro G, Zhou Z, Jiang T, Liu W, Li L, Bai Y, Quan P, Ding Y, Hirvonen J, Yin G, Santos HA, Fan J and Liu D. High drug-loaded microspheres enabled by controlled in-droplet precipitation promote functional recovery after spinal cord injury. Nat Commun 2022; 13: 1262.

[9] Zhou Y, Hou D, Marigo CC, Bonelli J, Rocas P, Cheng F, Yang X, Rocas J, Hamberg NM and Han J. Redox-responsive polyurethane-polyurea nanoparticles targeting to aortic endothelium and atherosclerosis. iScience 2022; 25: 105390.

[10] Thijs L, Quintens C, Vander Elst L, De Munter P, Depypere M, Metsemakers WJ, Vles G, Liesenborghs A, Neefs J, Peetermans WE and Spriet I. Clinical efficacy and safety of vancomycin continuous infusion in patients treated at home in an outpatient parenteral antimicrobial therapy program. Antibiotics (Basel) 2022; 11: 702.

[11] Dor E, David T, Dekel Jaoui H, Schwartz A, Baruchi T, Torgeman A, Ben David A, Rosen O, Tal A, Rosner A, Zichel R and Diamant E. A Rabbit model for prolonged continuous intravenous infusion via a peripherally inserted central catheter. Front Pharmacol 2021; 12: 637792.

[12] Schumacher M, Habibović P and van Rijt S. Peptide-modified nano-bioactive glass for targeted immobilization of native VEGF. ACS Appl Mater Interfaces 2022; 14: 4959-4968.

[13] Maishi N, Sakurai Y, Hatakeyama H, Umeyama Y, Nakamura T, Endo R, Alam MT, Li C, Annan DA, Kikuchi H, Morimoto H, Morimoto M, Akiyama K, Ohga N, Hida Y, Harashima H and Hida K. Novel antiangiogenic therapy targeting biglycan using tumor endothelial cell-specific liposomal siRNA delivery system. Cancer Sci 2022; 113: 1855-1867.

[14] Ha JM, Jin SY, Lee HS, Kum HJ, Vafaeinik F, Ha HK, Song SH, Kim CD and Bae SS. Akt1-dependent expression of angiopoietin 1 and 2 in vascular smooth muscle cells leads to vascular stabilization. Exp Mol Med 2022; 54: 1133-1145.

[15] Santonocito M, Zappulla C, Viola S, La Rosa LR, Solfato E, Abbate I, Tarallo V, Apicella I, Platania CBM, Maugeri G, D'Agata V, Bucolo C, De Falco S, Mazzone MG and Giuliano F. Assessment of a new nanostructured microemulsion system for ocular delivery of sorafenib to posterior segment of the eye. Int J Mol Sci 2021; 22: 4404.

[16] Papathanassiou M, Theodoropoulou S, Analitis A, Tzonou A and Theodossiadis PG. Vascular endothelial growth factor inhibitors for treatment of corneal neovascularization: a meta-analysis. Cornea 2013; 32: 435-444.
[17] Liu X, Wang S, Wang X, Liang J and Zhang Y. Recent drug therapies for corneal neovascularization. Chem Biol Drug Des 2017; 90: 653-664.
[18] Yao T, Chen H, Wang R, Rivero R, Wang F, Kessels L, Agten SM, Hackeng TM, Wolfs TGAM, Fan D, Baker MB and Moroni L. Thiol-ene conjugation of VEGF peptide to electrospun scaffolds as potential application for angiogenesis. Bioact Mater 2022; 20: 306-317.
[19] He M, Luo P, Xie Y, He Y, Wang X and Tan L. Electrochemical determination of vascular endothelial growth factor using functional metal-polymer nanocomposites. Colloids Surf A Physicochem Eng Asp 2023; 677: 132380.
[20] Liang K, Zhang R, Luo H, Zhang J, Tian Z, Zhang X, Zhang Y, Ali MK and Kong Q. Optimized attenuated salmonella typhimurium suppressed tumor growth and improved survival in mice. Front Microbiol 2021; 12: 774490.
[21] Tian W, Li J, Wang Z, Zhang T, Han Y, Liu Y, Chu W, Liu Y and Yang B. HYD-PEP06 suppresses hepatocellular carcinoma metastasis, epithelial-mesenchymal transition and cancer stem cell-like properties by inhibiting PI3K/AKT and WNT/β-catenin signaling activation. Acta Pharm Sin B 2021; 11: 1592-1606.
[22] Yang Z, Xiao H, Li X, Wei Z, Kang M, Wang R and Huang J. Antiangiogenic therapy with recombinant human endostatin may improve blood perfusion of cervical node with necrosis in nasopharyngeal carcinoma patients: a preliminary study by using contrast-enhanced ultrasound. Front Oncol 2025; 15: 1521762.
[23] Liao X, Yu X, Yu H, Huang J, Zhang B and Xiao J. Development of an anti-infective coating on the surface of intraosseous implants responsive to enzymes and bacteria. J Nanobiotechnology 2021; 19: 241.
[24] Jang D, Tang J, Schwendeman SP and Prausnitz MR. Effect of surface interactions on microsphere loading in dissolving microneedle patches. ACS Appl Mater Interfaces 2022; 14: 29577-29587.
[25] Cao L, Li Z, Song J, Xia X, Zhang G, Wang H and Zhao H. Sequential drug release system: targeting the tumor ECM for enhanced chemotherapy efficacy. Proc Natl Acad Sci U S A 2025; 122: e2421061122.
[26] Fontaine SD, Ashley GW, Houghton PJ, Kurmasheva RT, Diolaiti M, Ashworth A, Peer CJ, Nguyen R, Figg WD Sr, Beckford-Vera DR and Santi DV. A very long-acting PARP inhibitor suppresses cancer cell growth in DNA repair-deficient tumor models. Cancer Res 2021; 81: 1076-1086.
[27] Kim MW, Moon S, Park YI, Kim J, Kim SI and Lee R. Ultrasound-responsive lipid nanoparticles for targeted therapy and controlled drug release in non-small cell lung cancer. Adv Ther (Weinh) 2024; 7: 2400248.
[28] Shao T, Chen Z, Belov V, Wang X, Rwema SH, Kumar V, Fu H, Deng X, Rong J, Yu Q, Lang L, Lin W, Josephson L, Samir AE, Chen X, Chung RT and Liang SH. [(18)F]-Alfatide PET imaging of integrin αvβ3 for the non-invasive quantification of liver fibrosis. J Hepatol 2020; 73: 161-169.
[29] Li L, Liu N, Zhang H, Tao R, Zhao S, Chen Z, Fu Z, Li W, Xu L, Liu Y, Yu J and Yuan S. Potential (18)F-RGD PET/CT and DCE-MRI imaging-based biomarkers for postoperative survival prediction among patients with newly diagnosed glioblastoma treated with bevacizumab and chemoradiotherapy. Front Oncol 2022; 12: 848266.
[30] Krajcovicova S, Daniskova A, Bendova K, Novy Z, Soural M and Petrik M. [(68)Ga]Ga-DFO-c(RGDyK): synthesis and evaluation of its potential for tumor imaging in mice. Int J Mol Sci 2021; 22: 7391.
[31] Barkóczi A, Képes Z, Szabó JP, Dienes RA, Károlyi PK, Papp T, Kálmán-Szabó I, Sass T, Opposits G, Kertész I, Hajdu I, Trencsényi G and Deák Á. Metastasis and angiogenesis: preclinical PET study on hepatocellular carcinoma (He/De) tumor models. Eur J Pharm Sci 2025; 212: 107211.
[32] Chen J, Huang H, Zhong P, Lu Z, Ding X, Peng S, Zhu X, Wang F, Kong P, Tan AC, Song T, Xiao F and Chen L. Combining recombinant human endostatin with third-generation EGFR-TKIs in advanced EGFR-sensitive mutant non-small cell lung cancer. J Thorac Dis 2025; 17: 5223-5237.

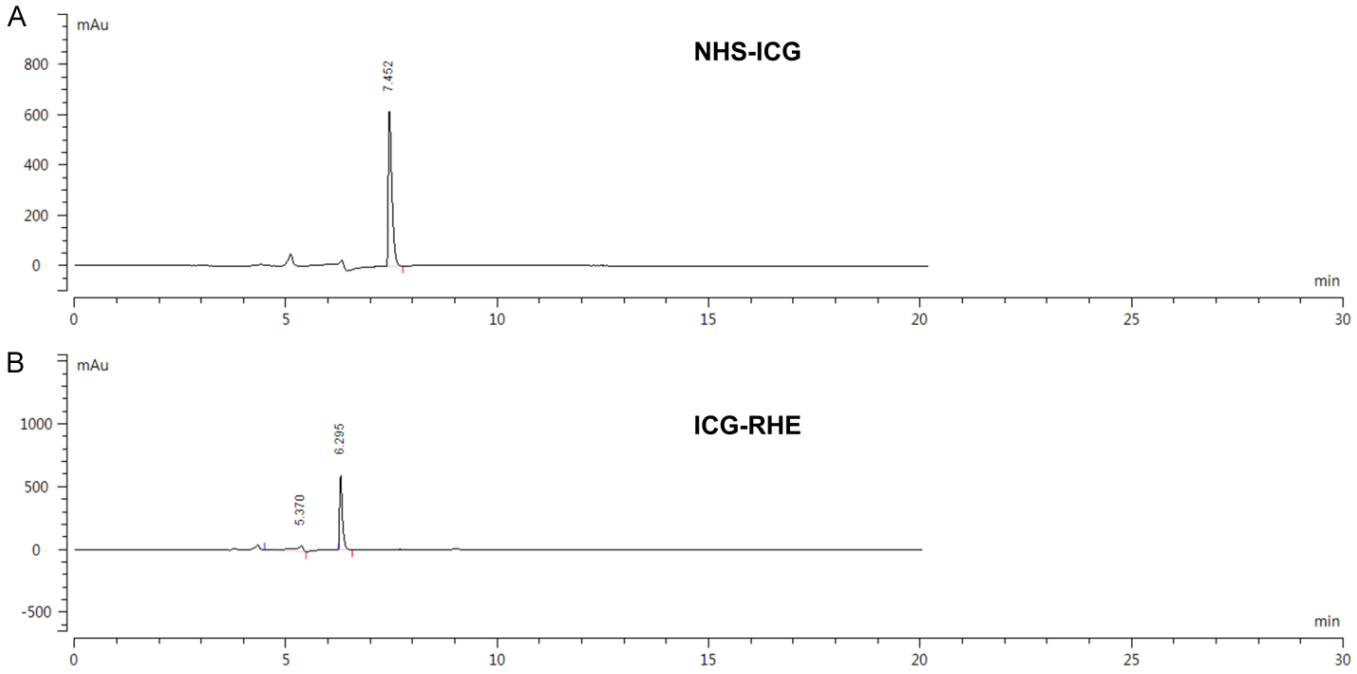

Figure S1. High-performance liquid chromatography profile of NHS-ICG (A) and ICG-RHE (B).